Available online at www.sciencedirect.com
SCIENCE DIRECT
Remote Sensing of Environment 100 (2006) 212 – 222
Remote Sensing of Environment
www.elsevier.com/locate/rse

Wildfire temperature and land cover modeling using hyperspectral data

Philip E. Dennison [a,*], Kraivut Charoensiri [a], Dar A. Roberts [b], Seth H. Peterson [b], Robert O. Green [c]

[a] Center for Natural and Technological Hazards, Department of Geography, University of Utah, Salt Lake City, UT 84112, United States
[b] Department of Geography and Institute for Computational Earth System Science, University of California Santa Barbara, Santa Barbara, CA 93106, United States
[c] Jet Propulsion Laboratory, California Institute of Technology, Pasadena, CA 91109, United States

Received 2 May 2005; received in revised form 18 October 2005; accepted 20 October 2005

Abstract

Wildfire temperature retrieval commonly uses measured radiance from a middle infrared channel and a thermal infrared channel to separate fire emitted radiance from the background emitted radiance. Emitted radiance at shorter wavelengths, including the shortwave infrared, is measurable for objects above a temperature of 500 K. The spectral shape and radiance of thermal emission within the shortwave infrared can be used to retrieve fire temperature. Airborne Visible Infrared Imaging Spectrometer (AVIRIS) data were used to estimate fire properties and background properties for the 2003 Simi Fire in Southern California, USA. A spectral library of emitted radiance endmembers corresponding to a temperature range of 500–1500 K was created using the MODTRAN radiative transfer model. A second spectral library of reflected solar radiance endmembers, corresponding to four vegetation types and two non-vegetated surfaces, was created using image spectra selected by minimum endmember average root mean square error (RMSE). The best fit combination of an emitted radiance endmember and a reflected solar radiance endmember was found for each spectrum in the AVIRIS scene. Spectra were subset to reduce the effects of variable column water vapor and smoke contamination over the fire. The best fit models were used to produce maps of fire temperature, fire fractional area, background land cover, land cover fraction, and RMSE. The highest fire temperatures were found along the fire front, and lower fire temperatures were found behind the fire front. Saturation of shortwave infrared channels limited modeling of the highest fire temperatures. Spectral similarity of land cover endmembers and smoke impacted the accuracy of modeled land cover. Sensitivity analysis of modeled fire temperatures revealed that the range of temperatures modeled within 5% of minimum RMSE was smallest between 750 and 950 K. Hyperspectral modeling of wildfire temperature and fuels has potential application for fire monitoring and modeling.

Keywords: Wildfire; Fire temperature; Radiance modeling; Airborne Visible Infrared Imaging Spectrometer (AVIRIS)

1. Introduction

Fire propagates through the combustion of fuels consisting of live and dead plant material. Fuel temperature must be high enough to volatilize and ignite these materials. Once ignition has occurred, the energy released through combustion raises the temperature of adjacent fuels. Pyne et al. (1996) links stages of combustion to temperatures at which they typically occur. As fuel temperature increases above 470 K, the volatilization of fuels begins, in a process called pyrolysis. Volatilized fuels can combust once the fuel temperature reaches 700–750 K. Flaming combustion typically occurs in wildland fuels between flame temperatures of 1070–1470 K, although maximum temperatures are believed to be as high as 2500 K. Smoldering combustion occurs at lower temperatures in denser fuels (Pyne et al., 1996).

As the temperature of the combusting fuels increases, the energy radiated by the fire increases and shifts to shorter wavelengths. By measuring thermal emission within multiple channels, remote sensing can be used to determine the dominant temperature of a fire. A temperature retrieval method developed by Dozier (1981) utilizes a middle infrared (MIR) channel and a thermal infrared (TIR) channel to separate the spectral contributions of fire and a cooler background. Planck functions for the fire thermal radiance and background thermal radiance are used to determine fire

* Corresponding author.
E-mail address: dennison@geog.utah.edu (P.E. Dennison).

0034-4257/$ - see front matter © 2005 Elsevier Inc. All rights reserved.
doi:10.1016/j.rse.2005.10.007

temperature and fire fractional area, the percent area of a fire within a pixel:

$$L_\lambda = f_{\text{fire}}\beta(\lambda, T_{\text{fire}}) + f_{\text{background}}\beta\left(\lambda, T_{\text{background}}\right) \quad (1)$$

where L_λ is the radiance at a specific wavelength λ, f_{fire} is the fire fractional area, $f_{\text{background}}$ is the background fractional area, $\beta(\lambda,T)$ is a Planck function, T_{fire} is the temperature of the fire and $T_{\text{background}}$ is the temperature of the background. The fire fractional area and background fractional area sum to 1. Eq. (1) exists for the spectral radiance in each channel, and for two or more channels the equations can be solved simultaneously to estimate fire temperature. Modifications of the Dozier (1981) technique have been used to retrieve fire temperature from Advanced Very High Resolution Radiometer (AVHRR) data (Matson & Holben, 1987), airborne radiometer data (Riggan et al., 2004), and Bi-spectral InfraRed Detection (BIRD) data (Oertel et al., 2004; Wooster et al., 2003; Zhukov et al., 2005). These approaches have used a small number of channels in the MIR and TIR to determine fire temperature.

The shortwave infrared (SWIR), the spectral region between 1100 and 2500 nm wavelength, can also be used for retrieving fire temperature. Unlike the MIR and TIR, the spectral contribution of background emitted radiance in the SWIR is minor. However, reflected solar radiance does make a significant contribution to the total measured radiance in the SWIR, even for hot fires. Like in the TIR and MIR, smoke has a relatively high transmittance in the SWIR. Green (1996) adapted the Dozier (1981) method to Airborne Visible Infrared Imaging Spectrometer (AVIRIS) radiance data that included the SWIR spectral region. AVIRIS collects 224 contiguous channels across an approximate spectral range of 370–2510 nm. Precise radiometric calibration of the AVIRIS instrument permits accurate quantification of at-sensor radiance (Green et al., 1998). The method proposed by Green (1996) models reflected solar radiance and two emitted blackbody radiances. The sum of these three radiances is fit to the spectral shape of the AVIRIS measured radiance using a non-linear least squares fitting routine.

This research expands on the method developed by Green (1996) for hyperspectral data. Reflected solar radiance and emitted radiance from a single source were summed and compared to AVIRIS measured radiance for a 2003 wildfire in Southern California. Radiance endmembers were used to create a linear spectral mixing model, and the best fit linear spectral mixing model was used to identify fire temperature and land cover within a fine spatial resolution AVIRIS scene. This research significantly improves the Green (1996) method by allowing multiple possible land cover endmembers. Simultaneous modeling of fire and fuel properties may allow improved modeling of fire behavior.

2. Background

The total spectral radiance measured by a sensor imaging a fire in daylight will be a combination of emitted radiance and reflected solar radiance. Atmospheric absorption and scattering of both emitted and reflected radiance (path radiance) must also be accounted for in the measured at-sensor radiance. Wavelength-specific, at-sensor radiance ($L_{\lambda t}$) can be expressed as a sum of the individual source radiances:

$$L_{\lambda \text{t}} = L_{\lambda \text{r}} + L_{\lambda \text{Pr}} + L_{\lambda \text{e}} + L_{\lambda \text{Pe}} \quad (2)$$

where $L_{\lambda \text{r}}$ is the reflected solar radiance, $L_{\lambda \text{Pr}}$ is the reflected solar path radiance, $L_{\lambda \text{e}}$ is the emitted radiance, and $L_{\lambda \text{Pe}}$ is the emitted path radiance. A single emission source is assumed. $L_{\lambda \text{r}}$ and $L_{\lambda \text{Pr}}$ are influenced by two-way transmission through the atmosphere, accounting for both the downwelling solar irradiance and the resulting upwelling reflected solar radiance. Assuming that the emission source is on the ground, $L_{\lambda \text{e}}$ and $L_{\lambda \text{Pe}}$ are solely upwelling radiance terms influenced by one way path transmittance through the atmosphere.

Emitted radiance is a function of temperature, emissivity, and atmospheric absorption and scattering. The emitted spectral radiance of a blackbody can be calculated using Planck's equation:

$$L_\lambda = \frac{2hc^2}{\lambda^5\left(e^{\frac{hc}{k\lambda T}} - 1\right)} \quad (3)$$

where T is the temperature in Kelvin, λ is the wavelength, c is the speed of light, h is Planck's constant, and k is Boltzmann's constant. The wavelength of peak radiance ($\lambda_{\max}$) for a blackbody can be determined by taking the derivative of Eq. (3):

$$\lambda_{\max} = \frac{a}{T} \quad (4)$$

where a is a constant equal to 2.898×10^{-3} K m. The total radiance for a blackbody can be determined by taking the integral of Eq. (3):

$$L = \frac{2k^4\pi^4T^4}{15h^3c^2} \quad (5)$$

Eqs. (4) and (5) show that as temperature increases, the wavelength of peak radiance shifts to shorter wavelengths and the total emitted radiance increases. Table 1 lists the

Table 1
Temperature, wavelength of peak radiance ($\lambda_{\max}$), total radiance (L) and radiance within the spectral region covered by AVIRIS (L_{AVIRIS})

Temperature (K)	$\lambda_{\max}$ (μm)	L (W m^{-2} sr^{-1})	L_{AVIRIS} (W m^{-2} sr^{-1})
288	10.06	1.24×10^{2}	4.09×10^{-4}
300	9.66	1.46×10^{2}	9.45×10^{-4}
400	7.24	4.62×10^{2}	1.58×10^{-1}
500	5.80	1.13×10^{3}	3.65×10^{0}
600	4.82	2.34×10^{3}	3.12×10^{1}
700	4.14	4.33×10^{3}	1.50×10^{2}
800	3.62	7.39×10^{3}	5.06×10^{2}
900	3.22	1.18×10^{4}	1.33×10^{3}
1000	2.90	1.80×10^{4}	2.96×10^{3}
1100	2.63	2.64×10^{4}	5.81×10^{3}
1200	2.41	3.74×10^{4}	1.04×10^{4}
1300	2.23	5.15×10^{4}	1.72×10^{4}
1400	2.07	6.93×10^{4}	2.68×10^{4}
1500	1.93	9.14×10^{4}	4.00×10^{4}

wavelength of peak radiance, the total radiance emitted, and radiance emitted within the portion of the spectrum measured by AVIRIS for a blackbody over a range of temperatures from 300 to 1500 K. The mean temperature of Earth's surface (288 K) is included for comparison. The spectral range measured by AVIRIS was assumed to be from the shorter half-maximum of the shortest wavelength channel (367 nm) to the longer half-maximum of the longest wavelength channel (2513 nm), using the 2003 configuration of the instrument.

The shift in the wavelength of peak radiance with increasing temperature demonstrates that spectral shape is an indicator of the temperature of an emitting body. Close to Earth's mean temperature, very little radiance occurs within the spectral range of AVIRIS. As temperature increases, the wavelength of peak radiance shifts from the MIR to the SWIR, and a larger percentage of the total radiance is emitted at wavelengths within the spectral range of AVIRIS. At temperatures above 1150 K, the wavelength of peak radiance falls within the spectral range of AVIRIS. Differences between the spectral shape of radiance emitted from thermal sources and the spectral shape of reflected solar radiance can be used to determine both the thermal contribution to the total radiance and the temperature of the emitting body (Green, 1996).

3. Data

Reflected and emitted radiance were modeled for an AVIRIS scene acquired over the 2003 Simi Fire in Southern California, USA. The Simi Fire was part of the catastrophic Southern California Fire Complex in October 2003. The combination of Santa Ana winds and low live fuel moisture promoted the rapid growth of seven large wildfires in Southern California. The Simi Fire was ignited on October 25, 2003 and consumed nearly 44,000 ha in the Santa Susana Mountains between ignition and full containment on November 5, 2003. The Simi Fire destroyed 315 structures and cost approximately $10 million to suppress (California Department of Forestry and Fire Protection, 2003).

Vegetation in the Santa Susana Mountains varies by slope, aspect, and elevation. Tall, dense stands of coast live oak are typically found close to streams and on north-facing, mesic slopes. Lower stature chaparral species, including chamise, scrub oak, and several species of *Ceanothus*, are found across a wide range of slopes and aspects at higher elevations. More xeric, lower elevations sites feature a mix of chaparral and coast sage scrub species, including sagebrush and sage. Grass and herb species are common in disturbed areas.

The AVIRIS instrument was flown over the Simi Fire on October 27, 2003 as the fire moved east through the Santa Susana Mountains. The data were acquired from the AVIRIS low-altitude platform, a Twin Otter airplane, from an altitude of 5.6 km above sea level. A scene containing the fire front was acquired between 1:01 PM and 1:11 PM Pacific Standard Time. The ground sample distance (spatial resolution) of the acquired scene was approximately 5 m. The 13.6 km long portion of this scene containing approximately 15 km of fire front and large areas of burned and unburned vegetation was used for this study. The AVIRIS scene was radiometrically calibrated (Green et al., 1998) and spatially corrected using onboard global positioning system and inertial data (Boardman, 1999). A false color composite using the 1682, 1107, and 655 nm channels of the AVIRIS scene (displayed as red, green, and blue, respectively) is shown (Fig. 1). In this composite, the fire is moving east and the wind direction is northeast. Vegetated areas appear green and burned areas appear dark gray. Smoke appears bright blue due to high reflectance in the 655 nm channel. Fire varies from red (cooler fires) to yellow (hotter fires) in Fig. 1.

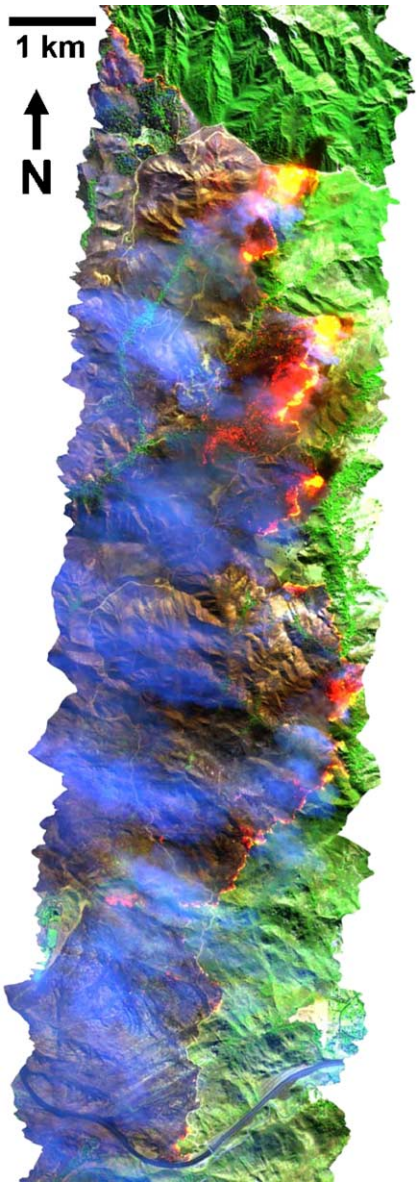

Fig. 1. A SWIR-NIR-red composite of the Simi Fire AVIRIS scene.

4. Methods

The reflected solar radiance measured by AVIRIS varies with surface reflectance, in contrast to solar path radiance which varies with atmospheric path length. To isolate reflected

solar radiance, AVIRIS scaled radiance data were corrected for solar path radiance using the atmospheric radiative transfer model MODTRAN (Berk et al., 1989). MODTRAN was used to model the expected solar path radiance given the mean height of the aircraft (5600 m), the mean elevation of the terrain in the scene (600 m), solar zenith and an assumed mid-latitude summer atmosphere with 23 km visibility. Atmospheric water vapor depth was retrieved by fitting the image with the absorption spectra of water vapor and liquid water (Green et al., 1993). The mean water vapor in the relatively smoke-free areas to the north and east of the fire, 822 atm-cm, was used to calculate path radiance. The resulting modeled path radiance spectrum was fit to sampled path radiance found in deeply shadowed areas of the scene, and then subtracted from each spectrum in the scene. Variation in solar path radiance due to differences in terrain height and spatial variability in column water vapor were not corrected.

With solar path radiance removed from the image, Eq. (2) becomes:

$$L_{\lambda m} = L_{\lambda r} + L_{\lambda e} + L_{\lambda Pe} \quad (6)$$

where $L_{\lambda m}$ is the solar path corrected radiance:

$$L_{\lambda m} = L_{\lambda t} - L_{\lambda Pr}. \quad (7)$$

Radiative transfer modeling can be used to model the emitted radiance and the emitted path radiance. If the reflection of emission by surfaces adjacent to the thermal source and atmospheric scattering of emitted radiance from adjacent thermal sources are ignored (adjacency effects), the emitted radiance and emitted path radiance can be assumed to be interdependent and combined into a single term:

$$L_{\lambda m} = L_{\lambda r} + L_{\lambda et} \quad (8)$$

where $L_{\lambda et}$ is the total emitted radiance.

Two modeling assumptions were made following Dozier (1981). First, the fire was assumed to be a blackbody emitter. Second, the fire within each AVIRIS image pixel was assumed to have a single temperature. The validity of these assumptions and potential errors introduced by these assumptions were addressed by Giglio and Kendall (2001). Eq. (8) can be expressed as a linear mixing model,

$$L_{\lambda m} = f_r L_{\lambda r} + f_{et} L_{\lambda et} + f_s L_s + \varepsilon \quad (9)$$

where f_r is the reflected solar radiance fraction and f_{et} is the fire fractional area. L_s is a shade radiance and f_s is a shade radiance fraction. The shade radiance is zero across all wavelengths and does not add to the measured radiance. The shade radiance and fraction allow the reflected solar radiance fraction and the fire fractional area to vary independently and allow the model equation to be solved using singular value decomposition. ε is an error term that accounts for any differences in spectral shape between the measured radiance ($L_{\lambda m}$) and the sum of the reflected solar radiance, emitted radiance, and shade radiance ($f_r L_{\lambda r} + f_{et} L_{\lambda et} + f_s L_s$). For all wavelengths, the residuals can be summed to calculate root mean square error (RMSE).

The reflected solar radiance fraction represents the relative reflectance of the image spectrum compared to the reflected solar radiance endmember. Fire fractional area represents the areal percentage of a pixel that is emitting the modeled radiance. Since linear mixing between fire emitted radiance and reflected solar radiance is assumed, the reflected solar radiance fraction, the fire fractional area, and the shade fraction are constrained to sum to 1.

Eq. (9) is a three-endmember linear spectral mixing model. Traditional spectral mixture analysis (SMA) uses fixed endmembers for all spectra in an image (Adams et al., 1993). SMA is inadequate for modeling reflected solar radiance or emitted radiance due to variation in surface composition and fire temperature. Multiple endmember SMA (MESMA) compares endmembers from a spectral library and determines the best combination of endmembers to fit each image spectrum (Roberts et al., 1998). The best combination of endmembers for each image spectrum is determined by the magnitude of the error term, ε. A lower error indicates a better fit to the modeled spectrum.

Image spectra were modeled using MESMA to find the best fit combination of a reflected solar radiance endmember, an emitted radiance endmember, and a shade endmember. The best fit endmembers for each image spectrum were selected from two spectral libraries, one spectral library containing the reflected solar radiance endmembers and a second spectral library containing emitted radiance endmembers. The reflected solar radiance endmembers were used to map land cover. These endmembers were selected from the image using Endmember Average RMSE (EAR; Dennison & Roberts, 2003a, 2003b). Endmembers were selected for six classes chosen based on their fuel characteristics, and included four vegetation classes (oak forest, dense chaparral, sparse chaparral/sage scrub, and grass) and two burned or unburnable surfaces (ash and soil/rock). Multiple polygons with apparent uniform composition were determined, totaling 200 image spectra for each class. EAR was used to determine the most-representative endmember for each land cover class. The six EAR-selected endmembers, one for each class, constitute the reflected solar radiance spectral library (Fig. 2a). Ash outside the area used to select the ash endmember was found to be brighter than the selected ash endmember. To increase the ability of the ash endmember to model ash in the AVIRIS image, the ash endmember radiance was multiplied by 1.25 across all wavelengths. The brightness-enhanced ash endmember is shown in Fig. 2a.

Asner and Lobell (2000) demonstrated that vegetation type and land cover in semiarid landscapes can be determined based on spectral shape in the SWIR. SWIR emitted radiance should also allow modeling of fire temperature, up to temperatures and fire fractional areas for which all SWIR channels are saturated. To reduce the impacts of smoke and water vapor, AVIRIS spectra were subset to omit visible and near infrared channels shorter than 1200 nm and channels within water vapor absorption bands. Smoke has low transmittance in the visible and near infrared, but transmittance increases from the near infrared through the SWIR. At wavelengths longer than 1200 nm, the contribution of smoke to total reflected solar radiance is small, except in shadowed areas where the background

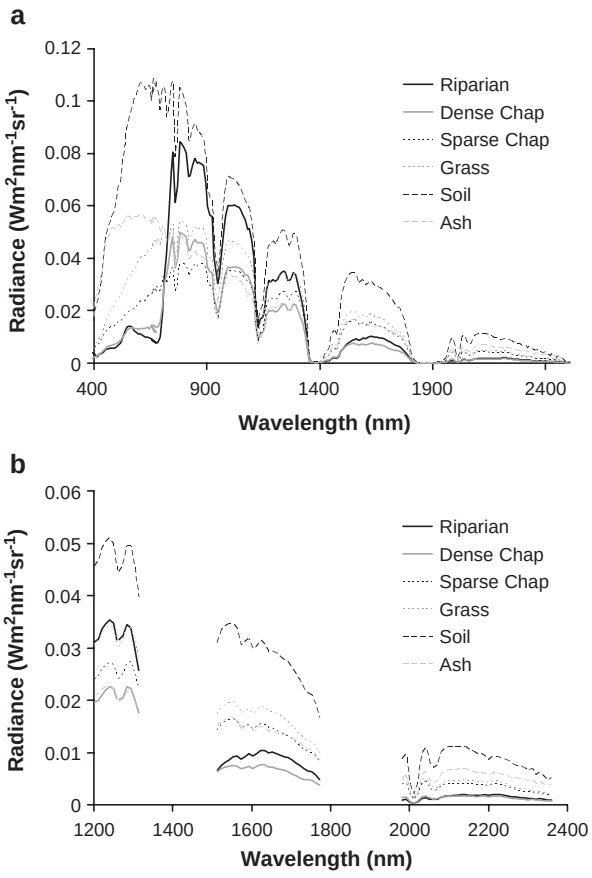

Fig. 2. The six reflected solar radiance endmembers selected using EAR, shown for the full spectrum (a) and for the set of wavelengths used for modeling (b).

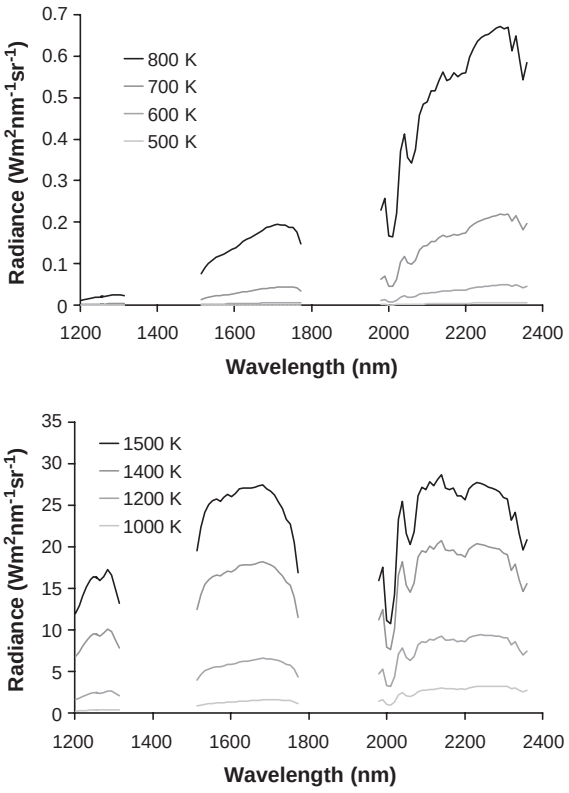

Fig. 3. Two subsets of the MODTRAN modeled emitted radiance library.

reflected solar radiance is very low. Variation in column water vapor also impacts measured radiance. Spatial variation in smoke and terrain elevation affects reflected solar and emitted radiance within SWIR water absorption bands. To reduce the impacts of smoke and water vapor, spectral mixing was modeled for a subset of AVIRIS channels. Omitted AVIRIS channels included:

- channels centered on wavelengths shorter than 1200 nm (channels 1–89)
- channels between 1320 and 1510 nm (channels 104–122)
- channels between 1775 and 1975 nm (channels 150–170)
- channels centered on wavelengths longer than 2365 nm (channels 210–224).

Fig. 2b shows the six EAR-selected endmembers for the subset of AVIRIS channels used for modeling.

The emitted radiance library was constructed from radiance endmembers modeled using MODTRAN. A temperature range of 500–1500 K (227–1227 °C) was selected for modeling, using 500 K as the probable lowest temperature at which pyrolysis would occur. Saturation of all SWIR channels was expected to occur at temperatures near 1500 K. Emitted radiance was modeled at increments of 10 K between 500 and 1500 K for the subset of AVIRIS channels (Fig. 3), creating a total of 101 emitted radiance endmembers. Parameters used in the MODTRAN emitted radiance calculations are listed in Table 2.

Both radiance spectral libraries were converted to AVIRIS encoded radiance. AVIRIS encoded radiance is equal to the radiance, in units of $\mu W\ cm^{-2}\ nm^{-1}\ sr^{-1}$, multiplied by a gain factor. For 2003 AVIRIS data, this gain factor was 500 for channels 1–160 and 1000 for channels 161–224. For each encoded radiance spectrum in the AVIRIS scene, all combinations of emitted radiance endmembers and reflected solar radiance endmembers were tested. Each AVIRIS image spectrum was tested for saturation, and only unsaturated channels were modeled. Singular-value decomposition was used to solve for the endmember fractions for each model, and RMSE was used to compare the fit of all models. Only models with land cover fraction and fire fractional area summing to between 0 and 1 were considered. Of these models, the single model with the lowest RMSE was selected for each image

Table 2
MODTRAN parameters for emitted radiance models

Parameter	Value
Spectral albedo	0
Atmosphere	Mid-latitude summer
Visibility	23 km
Date	October 27
Time	21.1028 GMT
Location	34.3527° N, 118.6463° W
Sensor altitude	5.6 km
Ground altitude	0.6 km
Water vapor	822 atm-cm
Carbon dioxide	375 ppm

spectrum, and the temperature, land cover class, and calculated endmember fractions for that model were assigned to each pixel. RMSE and residuals were not constrained.

A traditional accuracy assessment of land cover class mapping using ground reference data was not possible, since all the vegetation within the AVIRIS scene burned on October 27 or on subsequent days of the fire. Spectral shape and image context were used to identify 50 widely spaced pixels belonging to each land cover class within burned and unburned areas of the AVIRIS scene. The land cover map was compared to these reference data and used to construct an error matrix. Producer's accuracy, user's accuracy, overall accuracy, and Kappa coefficient (Cohen, 1960; Congalton, 1991) were calculated from the confusion matrix. No in situ fire temperature measurements were made for the Simi Fire, given the difficulty and danger of measuring the temperature of an actively burning wildfire. A MIR/TIR sensor might provide independent measurements of fire temperature. Unfortunately, no airborne or satellite sensors that might be able to provide these data were able to acquire imagery during the time the AVIRIS scene was acquired.

5. Results

The spectral mixing model assigned the best fit endmembers to each pixel within the AVIRIS scene. An example of a model fit for an unsaturated image spectrum is shown in Fig. 4a. A total of 606 endmember combinations were tested for each pixel, with 101 emitted radiance endmembers and 6 reflected solar radiance endmembers. The best fit model for this spectrum used the 910 K emitted radiance endmember and the ash reflected solar radiance endmember. The fire fractional area was modeled as 0.5% and the reflected solar radiance fraction was modeled as 32.3%. The remaining fraction (67.2%) was shade. RMSE in this example was 24.0 encoded AVIRIS radiance units.

Saturation of SWIR channels is dependent upon fire temperature and fire fractional area. As fire fractional area and temperature increase, the number of saturated channels also increases. The longest wavelength channels were first to saturate due to the shape of the emitted radiance curve. Fig. 4b shows an example of an AVIRIS spectrum saturated at wavelengths longer than 2020 nm. The model can only determine fit for wavelengths shorter than 2020 nm, reducing the number of channels used within the mixing model. The best fit model for this spectrum used the 790 K emitted radiance endmember and the ash reflected solar radiance endmember. The fire fractional area was modeled as 21.3% and the reflected solar radiance fraction was modeled as 58.0% for this example. The RMSE of this example was much higher, at 136.1 encoded AVIRIS radiance units.

The modeled endmembers were used to map fire temperature and land cover type within the AVIRIS scene. In areas where no fire was present, a high temperature endmember was mapped with an extremely low fire fractional area. In these cases, the emitted radiance endmember was being used to account for variation in the shape of the reflected solar

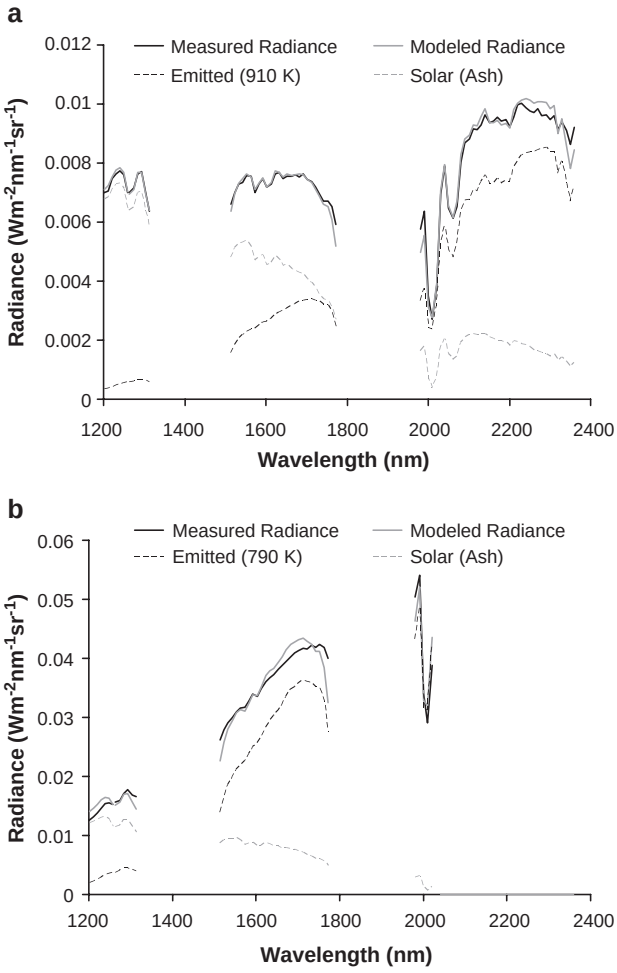

Fig. 4. Example fits for an unsaturated AVIRIS spectrum (a) and a saturated AVIRIS spectrum (b).

spectrum. A radiance threshold was used to separate burning and non-burning areas. Where the peak radiance of the emitted radiance endmember exceeded 100 AVIRIS encoded radiance units, the pixel was flagged as burning. Where the peak radiance of the emitted radiance endmember was less than 100 AVIRIS encoded radiance units, the pixel was flagged as non-burning. Lower encoded radiance thresholds flagged many non-burning areas as burning, while higher encoded radiance thresholds were found to miss burning areas along the fire front.

Fig. 5 shows the masked fire temperature and fire fractional area. In these images the fire is moving from left to right. Fire temperatures were highest within the fire front, where the fire is burning into new fuels. The hottest fires had a modeled temperature of 1500 K, but with a very low fire fractional area. Fires that either had a higher fire fractional area, or a higher fire temperature, are apparent in the unmodeled black centers of the northern fire front. These spectra were saturated throughout the modeled spectral range. The northern fire front was modeled as having higher temperatures than the southern fire front. Temperatures along the northern fire front were higher than 1100 K in many areas, while the southern fire front seldom reached this high temperature. Temperatures behind the fire

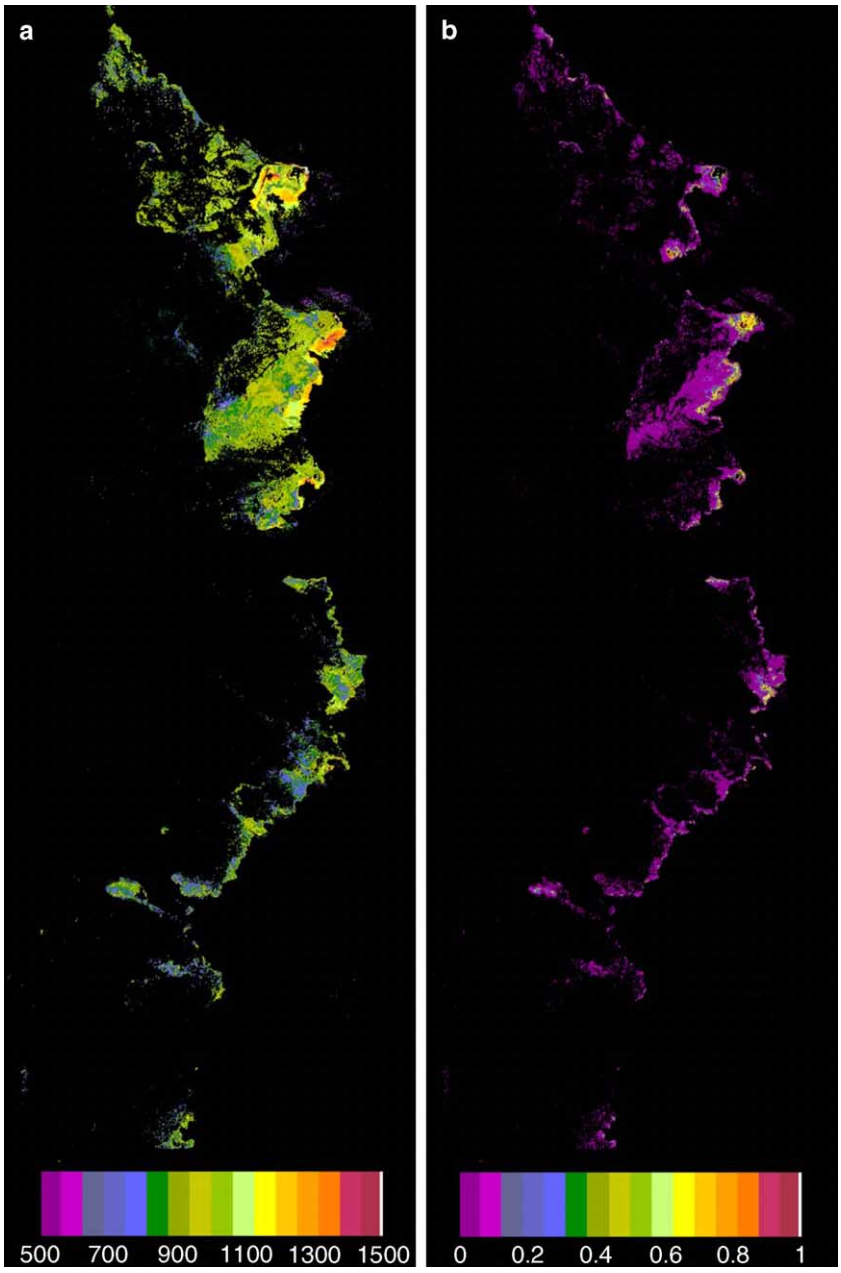

Fig. 5. Retrieved temperature ranging from 500 to 1500 K (a) and fire fractional area ranging from 0 to 1 (b).

front were modeled as much lower than temperatures within the fire front generally ranging from 800 to 1000 K along the northern fire front. Fire fractional area was below 10% in most areas of the fire (Fig. 5). Higher fire fractional area occurred primarily along the fire front, where fire fractional area was as high as 95%.

Land cover was mapped using the reflected solar radiance endmembers. Fig. 6a demonstrates a sharp difference between endmembers mapped within burned and unburned areas. Unburned areas within the AVIRIS scene were mostly modeled as one of four vegetation types: oak forest, dense chaparral, sparse chaparral, or grass. Oak forest and dense chaparral dominated in the higher elevation, mesic slopes in the northern half of the AVIRIS scene. Oak forest was also modeled in the riparian corridor on the right edge of the Fig. 6a. Sparse chaparral and grassland were modeled more frequently on lower elevation, xeric slopes in the southern half of the scene. Bare soil, rock outcroppings, and roads within the unburned areas of the scene were modeled with the soil/rock endmember.

The fire scar was mapped by the ash, soil/rock, and grass endmembers (Fig. 6a). Areas within the fire scar mapped by soil/rock and grass were consumed by the fire, so there should be no standing vegetation and ash should be the most likely land cover type. Areas mapped as soil/rock or grass within the fire scar all correspond to co-occurrence of smoke and either dark ash or shadows. The combination of smoke and a dark background, such as shadows or dark ash, created a spectral signature similar to soil or grass in the SWIR. Although the scattering caused by smoke in the SWIR was relatively minor,

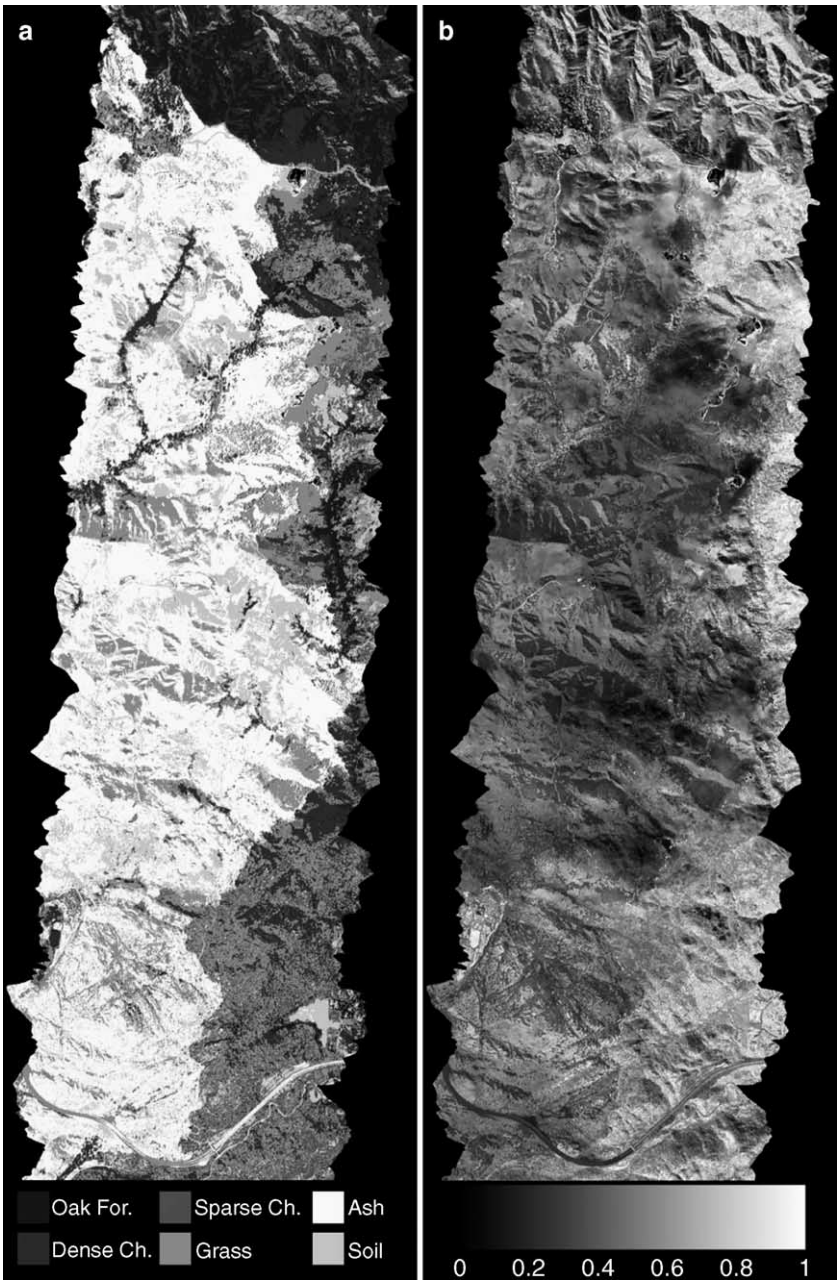

Fig. 6. The modeled reflected solar radiance endmember (a) and the fraction of that endmember, ranging from 0 to 1 (b).

for dark spectra the additional solar radiance reflected by smoke was enough to change the characteristic spectral shape of the background surface. A riparian corridor that was burned through, but still contained green vegetation, was mapped as a combination of dense chaparral and sparse chaparral rather than oak forest. The fire likely burned understory vegetation but apparently did not burn the upper portion of tree canopies within the riparian corridor. The standing vegetation may have been reduced enough to cause the riparian corridor to be mapped as dense and sparse chaparral. While most of the actively burning pixels within the image were modeled as ash, many of the saturated spectra were modeled as a different land cover type. The saturated spectra limited the number of channels that were used in the first step modeling of reflected solar radiance. The reduced number of channels sometimes led to ambiguity between the reflected solar radiance endmembers.

The reflected solar radiance endmember fraction was dependent on the mapped land cover type (Fig. 6b). Since each endmember possessed different mean radiances, shifts in the endmember fraction are visible where the endmember changes from one land cover type to another. Reflected solar radiance endmember fractions were highest for vegetated areas and brightly illuminated, south facing slopes. Reflected solar radiance endmember fractions were lowest for shadowed slopes and for dark ash surfaces.

Model RMSE was highest along the fire front (Fig. 7). Spectra that were modeled with the highest temperatures and fractional fire had the highest radiance, and correspondingly

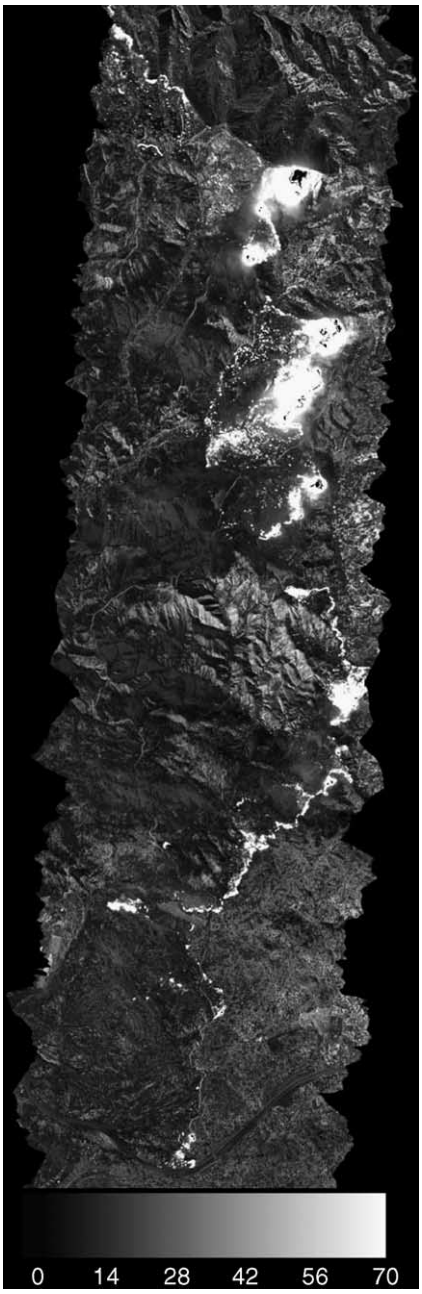

Fig. 7. Root mean square error for the best model fit, in AVIRIS encoded radiance.

had the highest RMSE. Within non-burning areas of the AVIRIS image, RMSE was highest for brightly illuminated slopes within the fire scar (Fig. 7).

The accuracy of the land cover map was assessed using 50 reference pixels belonging to each land cover class (Table 3). The overall accuracy of the land cover map based on the reference data was 68.0%, with a Kappa value of 0.62. Oak forest and soil/rock reference pixels had the highest producer's accuracy, with these two classes being mapped as the correct class in at least 45 of the 50 pixels. Grass reference pixels had the lowest Producer's accuracy, being mapped as grass only 21 pixels. Dense chaparral was most often confused with oak forest, sparse chaparral was most often confused with grass, and grass and ash were most often confused with soil/rock. In each case, the reference pixels were most likely to be mis-modeled as a spectrally similar endmember. If land cover classes are grouped into oak forest/dense chaparral, sparse chaparral/grass, and rock/soil/ash classes, overall accuracy climbs to 87.3%.

6. Discussion

While a quantitative assessment of fire temperature accuracy was not possible, there is an interesting correspondence between fire temperature, fire extent, and vegetation type. The hotter, larger fires in the northern half of the scene are moving primarily through dense chaparral. Cooler, smaller fires in the southern half of the scene are moving primarily though a mixture of dense chaparral, sparse chaparral and grass. Higher fuel loadings in dense chaparral would be expected to produce hotter, larger fires than sparse chaparral or grass. Few apparent "false positive" fire detections were located within the AVIRIS scene. Low temperature radiance spectra were mapped in two areas of dense chaparral directly in front of the hottest sections of the fire front. These areas do contain SWIR spectral signatures characteristic of emission from fires, but were vegetated and separated from the fire front. This emitted radiance could have been caused by sub-canopy fuels burning ahead of the fire front, or by reflected emitted radiance from the fire front. An examination of a digital elevation model of the area of the anomaly showed that these pixels possessed aspects that faced away from the fire front, and thus could not have been reflecting emitted radiance directly from the fire to the sensor. It is much more likely that the measured low temperature emitted radiance was due to small ground fires ahead of the main fire front.

A total of 170,556 pixels (8.9% of the AVIRIS scene) were modeled with a fire temperature based on radiance that exceeded the radiance threshold. The distribution of modeled fire temperatures is shown in Fig. 8. Relatively few pixels are modeled with fire temperatures below 750 K. The radiance threshold, while reducing the number of false detections, likely also causes the loss of pixels with low temperatures and low fractional area. The number of pixels modeled at each fire temperature peaks at 920 K, and then declines through 1490 K. The highest fire temperatures should be limited to the combustion of large amounts of unburned fuel along the fire front, so a decrease in the frequency of fires mapped at high temperatures was expected. Saturation of SWIR bands may further reduce the number of pixels modeled with high fire temperatures. The number of pixels mapped at 1500 K increases from the number of pixels mapped at 1490 K. This increase can be attributed to spectra that were nearly entirely saturated, but that had a few unsaturated channels that caused the pixel to be modeled with the highest possible fire temperature.

RMSE was used to quantify the sensitivity of modeled temperature. For each pixel, all three endmember models with RMSE within 5% of the minimum RMSE were compared. The set of endmember models with RMSE within 5% of the

Table 3
An error matrix comparing reference and modeled land cover for 50 pixels within each reference land cover class

		Reference land cover						User's
		Oak For.	Dense Ch.	Sparse Ch.	Grass	Soil	Ash	
Modeled land cover	Oak For.	45	22	0	0	0	0	0.67
	Dense Ch.	4	27	0	0	0	0	0.87
	Sparse Ch.	0	0	29	0	0	1	0.97
	Grass	1	1	20	21	3	2	0.44
	Soil	0	0	1	19	47	12	0.59
	Ash	0	0	0	10	0	35	0.78
Producer's		0.90	0.54	0.58	0.42	0.94	0.70	

minimum RMSE contained a range of temperatures, including a minimum and a maximum. The median minimum and maximum for all pixels modeled as a (minimum RMSE) temperature were then calculated (Fig. 8). For example, for the 6332 pixels that were best modeled by a three endmember model containing a 920 K emitted radiance endmember, the median minimum temperature modeled within 5% RMSE was 880 K, and the median maximum temperature modeled within 5% RMSE was 970 K. The range between the median minimum and maximum temperatures was smallest for modeled temperatures between 750 and 950 K, varying between 70 and 90 K. At both lower and higher temperatures, the range between the median minimum and maximum temperatures increased. Below a modeled temperature of 600 K, this range varied from 160 to 230 K. Above a modeled temperature of 1400 K, the range varied from 70 to 190 K.

RMSE of the modeled radiance may be increased by unmodeled adjacency effects. Adjacency effects will be highest in severely smoke-contaminated areas and in rugged terrain. The likely impact of adjacency effects would be an overestimation of temperature in cool regions adjacent to hot sources and an underestimation of the temperature of the hot source because of a loss of radiance to adjacent cooler pixels. However, because the wavelength specific nature of scattering is not perfectly correlated with the temperature of the source, the primary spectral shape of the source may still be preserved. In this case, the primary impact of adjacency effects would be an increase RMSE and a slight error in estimating the fire fractional area. While fully quantifying the extent of this error is beyond the scope of this paper, we have attempted to minimize adjacency effects by reducing the fit region to those spectral regions least impacted by smoke.

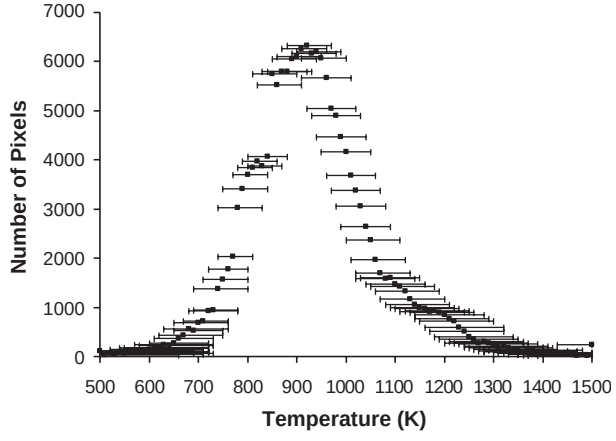

Fig. 8. The frequency of modeled fire temperatures from 500 to 1500 K, with error bars indicating the median range of temperatures modeled within 5% of the RMSE for the indicated temperature.

The range between the median minima and maxima indicates that the 10 K temperature increment used to model the emitted radiance component of SWIR spectra may be excessively small. Larger temperature increments, such as 50 K or 100 K, would still permit temperature modeling across a wide range of temperatures and would reduce the number of potential models, correspondingly decreasing computation time. Reliable modeling of pixels with high temperatures or high fire fractional areas will require the use of shorter near infrared and visible wavelengths. Addition of shorter wavelength channels would also likely improve the modeling of land cover. A spectral model of smoke would allow greater use of these wavelengths. A fourth smoke endmember may be able to model some of the spectral effects of smoke, but this endmember would have to account for both variable transmittance and reflectance of smoke.

7. Conclusions

High-resolution AVIRIS data were used to model fire temperature and background land cover for the 2003 Simi Fire. Using a previously underutilized spectral region, the SWIR, fire temperatures were mapped between 500 and 1500 K. A multiple endmember linear spectral mixing model was used to determine the best fit combination of emitted radiance and reflected solar radiance endmembers. Modeled temperature and land cover were consistent with known patterns of fire behavior and vegetation distribution, although SWIR saturation and smoke did produce errors.

The unique ability of hyperspectral data to retrieve both fire temperature and background land cover can be utilized by fire modeling. Vegetation type mapped ahead of the fire could be assigned to fuel classes. Fire positional information and fuel class, along with meteorological and terrain data, are sufficient for modeling fire spread using the current generation of operational predictive fire spread models (e.g. Finney, 1998). Additional fuel variables may be retrievable from active fire hyperspectral data. Depending on the level of smoke obscuration, NIR and SWIR channels may be used for determining canopy liquid water content, allowing quantitative assessment

of live fuel moisture during the fire (Dennison et al., 2003; Serrano et al., 2000; Ustin et al., 1998). Spectral mixture analysis can also provide relative fractions of live and senesced fuels (Dennison et al., 2000; Roberts et al., 2003). Fire spread models currently in development (e.g. Linn et al., 2002) can utilize more detailed fire and fuels information that can potentially be provided by hyperspectral data, including fire temperature, fuel type, and fuel moisture. Simultaneous fire and fuel information extracted using hyperspectral data could provide the basis for eventual real-time complex fire spread modeling.

Acknowledgments

Support for this research was provided by the Los Alamos National Laboratory Cooperative Agreement on Research and Education Program (SBB-0301A) and by a National Aeronautics and Space Administration (NASA) Regional Earth Science Application Center Grant (CSDH NASA RESAC 447633-59 075). We also thank the reviewers for their helpful comments.

References

Adams, J. B., Smith, M. O., & Gillespie, A. R. (1993). Imaging spectroscopy: Interpretation based on spectral mixture analysis. In C. M. Pieters, & P. A. J. Englert (Eds.), *Remote geochemical analysis: Elemental and mineralogical composition* (pp. 145–166). Cambridge, England: Press Syndicate of University of Cambridge.

Asner, G. P., & Lobell, D. B. (2000). A biogeophysical approach for automated SWIR unmixing of soils and vegetation. *Remote Sensing of Environment*, *74*, 99–112.

Berk, A., Bernstein, L. S., & Robertson, D. C. (1989). MODTRAN: A moderate resolution model for LOWTRAN7, AFGL-TR-89-0122, Hanscom Air Force Base, MA.

Boardman, J. W. (1999). Precision geocoding of low altitude AVIRIS data: Lessons learned in 1998. *Summaries of the Eighth JPL Airborne Earth Science Workshop*. *JPL Publication*, *vol. 99-17* (pp. 63–68). Pasadena: Jet Propulsion Laboratory.

California Department of Forestry and Fire Protection (2003). Incident Information. http://www.fire.ca.gov/cdf/incidents/Simi Incident_124/incident_info.html

Cohen, J. (1960). A coefficient of agreement for nominal scales. *Educational and Psychological Measurement*, *20*, 37–46.

Congalton, R. (1991). A review of assessment the accuracy of classifications of remotely sensed data. *Remote Sensing of Environment*, *37*, 35–46.

Dennison, P. E., & Roberts, D. A. (2003a). Endmember selection for multiple endmember spectral mixture analysis using Endmember Average RMSE. *Remote Sensing of Environment*, *87*, 123–135.

Dennison, P. E., & Roberts, D. A. (2003b). The effects of vegetation phenology on endmember selection and species mapping in Southern California chaparral. *Remote Sensing of Environment*, *87*, 295–309.

Dennison, P. E., Roberts, D. A., & Regelbrugge, J. C. (2000). Characterizing chaparral fuels using combined hyperspectral and synthetic aperture radar. *Proceedings of the Ninth JPL Airborne Earth Science Workshop, Pasadena: Jet Propulsion Laboratory. JPL Publication*, *vol. 00–18* (pp. 119–124).

Dennison, P. E., Roberts, D. A., Thorgusen, S. R., Regelbrugge, J. C., Weise, D., & Lee, C. (2003). Modeling seasonal changes in live fuel moisture and equivalent water thickness using a cumulative water balance index. *Remote Sensing of Environment*, *88*, 442–452.

Dozier, J. (1981). A method for satellite identification of surface temperature fields of subpixel resolution. *Remote Sensing of Environment*, *11*, 221–229.

Finney, M. A. (1998). FARSITE, Fire Area Simulator-model development and evaluation, U.S. Dept. of Agriculture Forest Service Rocky Mountain Research Station Research Paper RMRS RP-4, Ogden, UT.

Giglio, L., & Kendall, J. D. (2001). Application of the Dozier retrieval to wildfire characterization — A sensitivity analysis. *Remote Sensing of Environment*, *77*, 34–49.

Green, R. O. (1996). Estimation of biomass fire temperature and areal extent from calibrated AVIRIS spectra. *Summaries of the Sixth Annual JPL Airborne Earth Science Workshop*. *JPL Publication 96-4*, *vol. 1* (pp. 105–113). Pasadena: Jet Propulsion Laboratory.

Green, R., Conel, J., & Roberts, D. (1993). Estimation of aerosol optical depth and additional atmospheric parameters for the calculation of apparent surface reflectance from radiance as measured by the Airborne Visible-Infrared Imaging Spectrometer (AVIRIS). *Summaries of the Fourth Annual JPL Airborne Geosciences Workshop*. *JPL Publication 93-26*, *vol. 1* (pp. 73–76). Pasadena: Jet Propulsion Laboratory.

Green, R. O., Eastwood, M. L., Sarture, C. M., Chrien, T. G., Aronsson, M., Chippendale, B. J., et al. (1998). Imaging spectroscopy and the Airborne Visible Infrared Imaging Spectrometer (AVIRIS). *Remote Sensing of Environment*, *65*, 227–248.

Linn, R., Reisner, J., Colman, J. J., & Winterkamp, J. (2002). Studying wildfire behavior using FIRETEC. *International Journal of Wildland Fire*, *11*, 233–246.

Matson, M., & Holben, B. (1987). Satellite detection of tropical burning in Brazil. *International Journal of Remote Sensing*, *8*, 509–516.

Oertel, D., Zhukov, B., Thamm, H. P., Roehrig, J., & Orthmann, B. (2004). Space-borne high resolution fire remote sensing in Benin West Africa. *International Journal of Remote Sensing*, *25*, 2209–2216.

Pyne, S. J., Andrews, P. L., & Laven, R. D. (1996). *Introduction to wildland fire*. New York: Wiley.

Riggan, P. J., Tissell, R. G., Lockwood, R. N., Brass, J. A., Pereira, J. A. R., Miranda, H. S., et al. (2004). Remote measurement of energy and carbon flux from wildfires in Brazil. *Ecological Applications*, *14*, 855–872.

Roberts, D. A., Dennison, P. E., Gardner, M. E., Hetzel, Y., Ustin, S. L., & Lee, C. T. (2003). Evaluation of the potential of Hyperion for fire danger assessment by comparison to the Airborne Visible/Infrared Imaging Spectrometer. *IEEE Transactions on Geoscience and Remote Sensing*, *41*, 1297–1310.

Roberts, D. A., Gardner, M., Church, R., Ustin, S., Scheer, G., & Green, R. O. (1998). Mapping chaparral in the Santa Monica Mountains using multiple endmember spectral mixture models. *Remote Sensing of Environment*, *65*, 267–279.

Serrano, L., Ustin, S. L., Roberts, D. A., Gamon, G. A., & Penuelas, J. (2000). Deriving water content of chaparral vegetation from AVIRIS data. *Remote Sensing of Environment*, *74*, 570–581.

Ustin, S. L., Roberts, D. A., Pinzon, J., Jacquemoud, S., Gardner, M., Scheer, G., et al. (1998). Estimating canopy water content of chaparral shrubs using optical methods. *Remote Sensing of Environment*, *65*, 280–291.

Wooster, M. J., Zhukov, B., & Oertel, D. (2003). Fire radiative energy for quantitative study of biomass burning: Derivation from the BIRD experimental satellite and comparison to MODIS fire products. *Remote Sensing of Environment*, *86*, 83–107.

Zhukov, B., Briess, K., Lorenz, E., Oertel, D., & Skrbek, W. (2005). Detection and analysis of high-temperature events in the BIRD mission. *Acta Astronautica*, *56*, 65–71.